

LA-UR-21-24964

Approved for public release; distribution is unlimited.

Title: Demonstration of Advanced Experimental and Theoretical
Characterization of Hydrogen Dynamics and Associated Behavior in
Advanced Reactors

Author(s): Trellue, Holly Renee; Vogel, Sven C.; Long, Alexander Makenzie; Mehta,
Vedant Kiritkumar; Armstrong, Jerawan Chudoung; Mckinney, Gregg
Walter; Shivprasad, Aditya Prahlad; Luther, Erik Paul; Cooper, Michael
William Donald; Wilkerson, Robert Blake; Payne, Joshua Estes; Carver,
Dale Travis; Rising, Michael Evan; Bull, Jeffrey S.; Kulesza, Joel A.

Intended for: Report

Issued: 2021-05-24

Disclaimer:

Los Alamos National Laboratory, an affirmative action/equal opportunity employer, is operated by Triad National Security, LLC for the National Nuclear Security Administration of U.S. Department of Energy under contract 89233218CNA000001. By approving this article, the publisher recognizes that the U.S. Government retains nonexclusive, royalty-free license to publish or reproduce the published form of this contribution, or to allow others to do so, for U.S. Government purposes. Los Alamos National Laboratory requests that the publisher identify this article as work performed under the auspices of the U.S. Department of Energy. Los Alamos National Laboratory strongly supports academic freedom and a researcher's right to publish; as an institution, however, the Laboratory does not endorse the viewpoint of a publication or guarantee its technical correctness.

Demonstration of Advanced Experimental and Theoretical Characterization of Hydrogen Dynamics and Associated Behavior in Advanced Reactors

by Holly Trellue¹, Sven Vogel², Alex Long², Vedant Mehta¹, Jerawan Armstrong³,
Gregg McKinney¹, Aditya Shivprasad², Erik Luther⁵, Mike Cooper², Blake Wilkerson¹,
Joshua Payne⁴, D. Travis Carver², Mike Rising³, Jeff Bull³, Joel Kulesza³

Los Alamos National Laboratory
LA-UR-xx

¹*Nuclear Engineering and Nonproliferation (NEN)*

²*Materials Science and Technology (MST)*

³*X-Computational Physics (XCP)*

⁴*Computer, Computational, and Statistical Sciences (CCS)*

⁵*Sigma Division*

Abstract

Advanced materials development, manufacturing, and modeling capabilities for innovative reactor designs support nuclear security and mission-focused science through enhanced technology for safer and more efficient and secure production of nuclear energy. The research in this project has established: 1) a state-of-the-art neutron-based hydrogen mapping and cross-section measurement capability as well as detailed crystallographic characterization of hydrogen atoms at LANSCE, and 2) a multi-physics framework for simulating behavior of moderator materials and other material performance in advanced nuclear reactors. Through the course of this project, we successfully developed and demonstrated measurement techniques for hydrogen distribution and atomistic-scale behavior of hydrogen atoms using pulsed neutron techniques. In parallel, advanced multi-physics simulation tools to predict the behavior of hydrogen atoms, e.g. in a moderator for a nuclear reactor, through materials performance, neutron transport, and thermal mechanical behavior were enhanced. Multi-discipline areas across the laboratory were involved in the project as the integration of improved experimental capabilities with enhanced modeling and simulation through MST, NEN, SIGMA, and XCP division subject matter experts.

1.0 Introduction

The research performed in this project demonstrates that we have successfully: 1) characterized behavior such as neutron diffraction and movement of hydrogen in yttrium hydride ($\text{YH}_{x,x=1.3-2.0}$) moderators at high temperatures through experiments at the Los Alamos National Science Center (LANSCE), and 2) developed a framework for analyzing multi-physics performance on small geometric scales using improvements in the Monte Carlo N-Particle[®] (MCNP[®]) transport code for advanced reactor applications. The purpose of moderating material in a small reactor such as a microreactor is to thermalize (slow down) neutrons, increasing the probability of fission and decreasing the required fuel mass. Hydrides are efficient moderators but are subject to the movement of hydrogen at high enough operating temperatures. Thus, analysis of hydrogen movement is important for reactor applications using one of two different hydride materials currently being researched: yttrium and zirconium hydride [1] [2]. The advantage of yttrium hydride is that it retains hydrogen at higher temperatures (i.e. greater than 500°C) than zirconium hydride (see Fig. 1), which increases the allowable operating temperature of a system and thus the efficiency and reliability of power generation. The drawback to yttrium hydride material compared to zirconium hydride is that yttrium, which is monoisotopic in nature as Y-89, has a thermal neutron absorption cross-section that is approximately one order of magnitude larger than that of natural zirconium (1.28 barns vs. 0.185 barns for thermal neutrons, <https://www.ncnr.nist.gov/resources/n-lengths/>) [3]. In addition, yttrium hydride is not as well characterized as zirconium hydride. The goal of this LDRD project is to measure diffraction and diffusion responses of hydrogen in YH_x and track the effects through predictive modeling capabilities (see Fig. 2) to better understand the performance of this promising moderator material. Details of the experimental and theoretical work performed are given in Section 3. Our team consists of reactor modelers, nuclear engineers, solid state physicists, neutron diffraction, and neutron imaging experts all integrating knowledge together to understand performance of moderator materials.

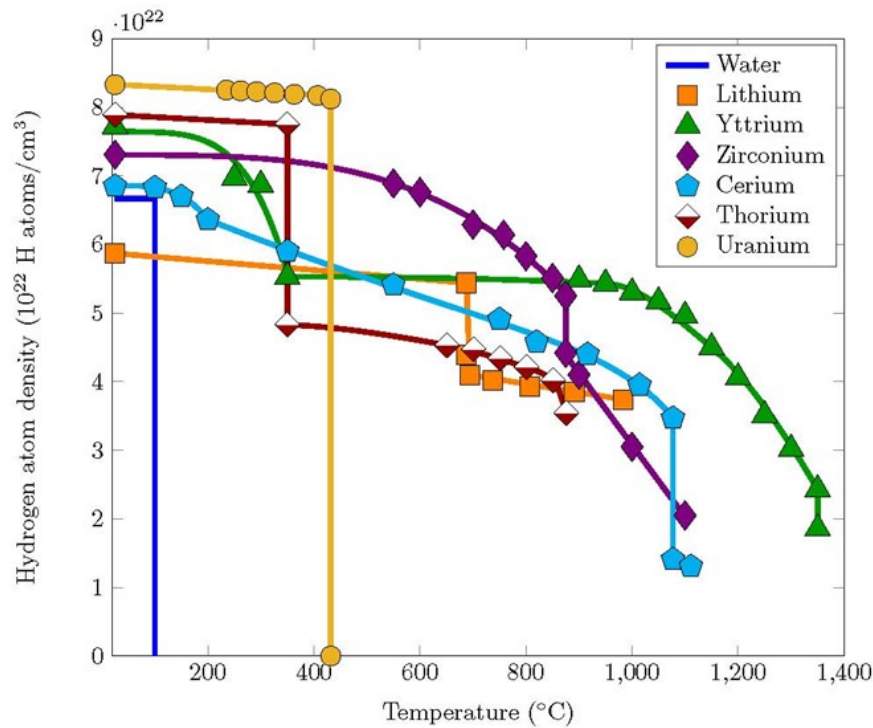


Figure 1. Hydrogen retention as a function of temperature for various hydrides.

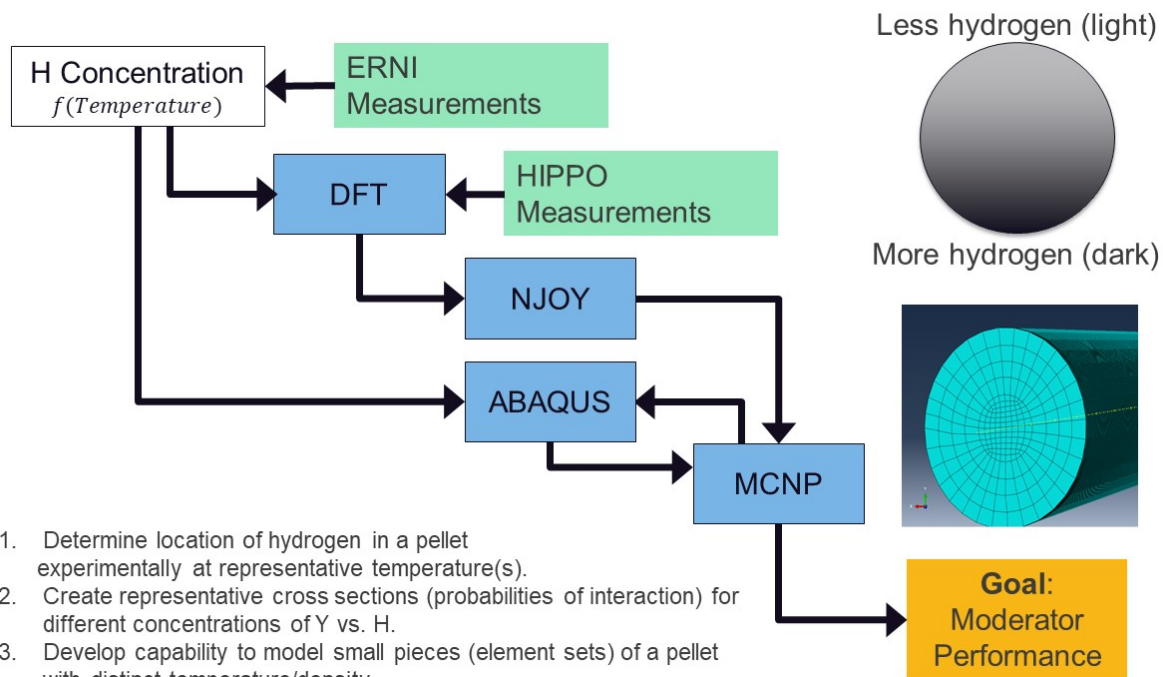


Figure 2. Flow Diagram for Integrating Experimental and Theoretical Research

2.0 Objective and Background

Innovative nuclear reactor designs are currently being proposed to increase efficiency and economic viability of nuclear energy production. Microreactors are an emerging new nuclear technology around the world with a power of about 0.1-20 MWt (0.03-6 MWe) to provide small,

mobile power sources in applications such as remote environments [4]. The compactness of a microreactor leads to different types of fuel, coolant, and system needs than larger commercial light water reactors. In support of these designs, solid moderator materials such as yttrium hydride provide reductions in the size and fuel mass requirements of the system and avoid complications with a liquid coolant such as water. However, hydrogen is a highly mobile element that will not remain homogeneous through time and irradiation. For example, the stoichiometry will change as a function of temperature and radial location within the material, and this effect should be included in predictive simulations. Understanding hydrogen dynamics, i.e. the behavior of hydrogen atoms in materials as a function of temperature and hydrogen concentration, is of paramount importance to assess moderator efficiency and thus overall reactor performance of these and related systems. ***Determining experimentally how the hydrogen changes within a material to close the gap in available data combined with developing a simulation framework to easily model the variations on a small, individual elemental basis within a material more easily and predict the influence of these variations on the moderator performance are the objectives of this project.*** The experimental capabilities demonstrated as part of this project can be applied to numerous types of hydride materials in a variety of future applications. In addition, the improved multi-physics framework will be applied to various nuclear system simulations requiring fine-mesh/detailed elemental analysis. In particular, goals of this project included:

- Combine experiment and simulations to improve understanding of moderator performance.
- Validate stability of high temperature moderator material so it can be applied to future applications.
- Publish results as appropriate and socialize the ideas with vendors and licensing agencies.
- Design and implement hydrogen mapping experiments in particular for quality assurance and licensing in a reactor.

2.1 Methodology for Experimental Research

There are currently a wide range of neutron radiography capabilities at LANL that have been and are still being developed utilizing available neutron spallation sources at the Los Alamos Neutron Science Center (LANSCE). These capabilities range from fast neutron imaging at the Weapons Neutron Research (WNR) facility, to energy-resolved neutron imaging and phase contrast imaging at the Lujan Center (see [5] and references therein). Through this project, we demonstrated a novel capability for spatially measuring hydrogen movement (diffusion) in yttrium hydride samples as a function of both temperature and stoichiometry on the Energy-Resolved Neutron Imaging (ERNI) flight path 5 (FP5) at the Lujan Center. We assessed advantages of extracting neutron attenuations at different neutron wavelengths/energies recorded during a single measurement. Access to this type of information allows us to select energy regions where attenuation contrast due to hydrogen is maximized and attenuation due to other isotopes present is minimized. Exploiting the capability for hydrogen mapping had, to the best of our knowledge, not been attempted at pulsed neutron radiography facilities elsewhere. Over the past several years novel techniques of spatially-resolved hydrogen concentration measurements

via neutron radiography have been developed, and well established, at neutron radiography facilities such as the ICON facility at SINQ (PSI), ANTARES -II at FRMII (TUM), along with several other reactor-based neutron facilities [6, 7, 8, 9, 10, 11, 12, 13]. These sources have similar neutron intensities as those available at LANSCE, allowing us to expect similar performance. Spatially-resolved hydrogen mapping via neutron radiography is a relatively unique probe as it is both nondestructive (sample is not compromised) and a complete bulk (not just at the surface) measurement. Furthermore, this method can be expanded upon by using pixelated neutron imaging detectors, where neutron attenuation coefficients are determined on a pixel-by-pixel bases, thus allowing for spatially-resolved hydrogen mapping in 2D (and possibly 3D). The application of ERNI to spatially measure H-concentrations has been developed previously at the ISIS Facility in the United Kingdom and has been successfully proven to measure H-concentrations in ZH_x down to a resolution of 8-14 wt% ppm of H [7]. Promising results from studies like those in Ref. 7 led to the development of similar capabilities on FP5 at LANSCE. The results helped us understand hydrogen distributions in YH_x material as a function of radius, temperature, and stoichiometry and the effect on neutron multiplication, which led to a greater understanding of performance of a microreactor system at high temperatures. As part of the project, we also improved the current energy-resolved capabilities at the ERNI flight path with a new high fidelity camera and two-zone furnace for generating temperature gradients on samples being analyzed.

In addition, using measured results, we investigated the relationship between lattice parameters and stoichiometry in yttrium hydride as an additional, and independent, method of examining hydrogen distributions in yttrium hydride. In order to achieve this, measurements were split up into two components: First, spatially resolved measurements of lattice parameters in yttrium hydride samples were performed on the ERNI flight path using Bragg edge radiography techniques. This type of techniques relies on observing so-called Bragg-edges occurring in the transmission spectra at the neutron wavelengths equivalent to twice the lattice spacing ($\lambda=2d$). At these conditions, neutrons are no longer attenuated by diffraction off lattice planes, and the transmission exhibits a sharp increase (edge) just above the specific wavelength. Bragg edge radiography has proven to be a powerful probe in extracting lattice parameters in materials such as steels and other metal alloys [14, 15, 16], though to the best of our knowledge this technique had not be applied to hydrogenous materials in particular. Second, diffraction experiments on the HIPPO/FP4 beam line allowed us to examine and establish the dependence of yttrium hydride lattice parameters as a function of stoichiometry. Using Rietveld analysis techniques, information such as lattice parameters, atomic positions, bond lengths, anisotropic atomic displacement parameters, and site occupation factors can all be extracted as a function of temperature and stoichiometry. This type of data allows to benchmark crystal structure predictions, which has been for example applied to nuclear fuels (e.g. U_3Si_2) and ceramics (so-called MAX phases). These type of diffraction measurements have been demonstrated on HIPPO in the past on batteries [17, 18], hydrogen storage materials [19] as well as hydrogen-bearing minerals [20, 21, 22] and phases occurring in concrete and high explosives [23, 24]. Combining the information extracted from these two techniques provides us with independent spatial measurements of stoichiometry distributions (along with other information related to lattice parameters) in a given yttrium hydride sample.

2.2 Methodology for Theoretical Work

From the Bragg edge radiography and the neutron diffraction measurement results, atomic scale simulations using the density-functional theory (DFT) code VASP were used to investigate a range of material properties, for example on YH_2 and YH_{2-x} . Characteristics such as elastic constants, specific heat capacity, lattice parameter, phonon density of states, phonon dispersion curves, and electronic density of states of YH_2 are among those commonly analyzed and compared with available experimental and modeling literature data [25-28]. Simulations on the behavior of point defects in YH_2 in this research were performed to analyze hydrogen vacancies. Nudged elastic band simulations were combined with phonon calculations to predict the diffusivity of H point vacancies in YH_2 . Following this, predictions were made about the point defect limit to investigate thermo-physical and diffusional properties for compositions ranging from $\text{YH}_{1.3}$ - YH_2 . The phonon densities of states produced by DFT were used as input for the cross section processing code NJOY to determine the $S(\alpha, \beta)$ thermal scattering probability laws for YH_{2-x} , with the predictions for YH_2 already obtained and verified against literature data. The resulting new cross sections produced by NJOY can be input into the Monte Carlo N-Particle[®] (MCNP[®]) transport code [29].

The MCNP code is developed and maintained at LANL and has become a ‘gold standard’ in radiation transport for many applications, including: radiation detection, nuclear security, reactor performance, and more. The MCNP code has the ability to externally link to other multi-physics tools such as Abaqus for thermal mechanical behavior and CINDER90 for isotope generation and depletion calculations. However, the MCNP code has been limited in its capabilities to produce data easily for both thermal mechanical and deterministic tools to assess predictive performance of multi-physics, transient (short time-scale), and other multi-group data for physics simulations. For instance, elemental densities and temperatures from Abaqus unstructured mesh models were not previously used in MCNP calculations. We developed a new computational framework for Abaqus/MCNP linked simulations [30, 31]. The linkage between MCNP and Abaqus simulations now includes not only geometric changes, but also variations in temperature and density in the MCNP input file based on Abaqus calculations plus the ability to add distributions obtained from experimental results. Additionally, the MCNP code has been improved by outputting results of multi-group cross sections, velocities, and scattering moments required for deterministic time-dependent simulations of reactivity. The resulting improvements significantly enhance our ability to model small differences in systems due to hydrogen distribution or other effects.

3.0 Results

The specific tasks accomplished in this LDRD project included four main areas with the specific subtasks listed below that will be discussed in subsequent sections.

1. Performed hydrogen concentration and stoichiometry measurements
 - 1.1 Spatially mapped out hydrogen distributions by measuring attenuation coefficients via ERNI
 - 1.2 Spatially mapped YH stoichiometry distributions

- 1.2.1 Established relations between stoichiometry and lattice parameters with neutron diffraction from the HIPPO measurements
 - 1.2.2 Preliminarily mapped out lattice parameters via Bragg Edge Radiography
- 2. Conducted hydrogen diffusion measurements
 - 2.1 Spatially mapped hydrogen concentrations in YH_x samples at varying temperatures.
 - 2.2 Determined thermal conductivity and diffusivity as a function of stoichiometry
- 3. Characterized point defects and other parameters of YH_x
 - 3.1 Modeled hydrogen materials with density functional theory codes and verified predictions with high resolution crystal analysis and diffraction.
 - 3.2 Evaluated atomic scale results on point defect behavior in YH_x as a function of stoichiometry.
 - 3.3 Developed an approach for experimentally obtaining thermal scattering cross sections with differential die away techniques.
- 4. Developed an automated multi-physics framework for advanced reactor analysis with the Monte Carlo N-Particle transport (MCNP®) code linked to the thermal mechanical analysis code Abaqus
 - 4.1 Modified the MCNP code to input densities and temperatures individually for each element set within an Abaqus unstructured mesh model.
 - 4.2 Generated new tally options within the MCNP code to extract information for time-dependent kinetic calculations with deterministic transport codes
 - 4.3 Created an Abaqus-MCNP framework for automated neutronic-thermal multi-physics calculations.

Five journal articles describe detailed results of Tasks 1 through 3 have been or will soon be published. A conference paper was and other papers were written/presented on Task 4, describing the new methodologies that were added to the MCNP code suite.

3.1. Measuring H concentrations and stoichiometry

Understanding the distribution of hydrogen in a given YH_{2-x} material is critical to evaluating its potential performance as a moderating material in future reactor designs. We performed preliminary measurements employing Energy Resolved Neutron Imaging (ERNI) techniques and the HIPPO instrument with the goal of observing effects of varying hydrogen concentration in YH_{2-x} samples fabricated at the SIGMA building at LANL and other samples. The key concept in this capability is utilizing neutron attenuation spectra taken with neutron transmission measurements and then relating hydrogen densities to well-characterized samples with a known pedigree. To date most studies have selected a sub-set from all the samples measured and used destructive techniques to independently measure H-concentrations, so our work proves a unique concept for obtaining such information more directly. To that effect, we first performed several proof-of-principle measurements to understand Bragg edge effects and to demonstrate the ability of neutron radiography to produce images of hydrogen concentrations as a function of stoichiometry at ambient conditions. Then we performed neutron diffraction measurements to assess lattice parameters and crystallographic characterization of yttrium hydride with different

hydrogen stoichiometries. Results informed subsequent calculations of scattering cross sections (interaction probabilities).

3.1.1 Measurements on Flight Path 5 at LANSCE

FP5 is located on the 1L neutron spallation target of the Lujan Center at LANSCE. The 1L target is operated at 20 Hz and provides a high intensity neutron flux, via a high intensity moderator, to the FP5 beamline with neutron energies ranging from low thermal to high epi-thermal [5]. The typical neutron energy spectra for FP5, along with some other facilities at LANSCE is shown in Figure 3. This neutron flux has a large thermal component making FP5 an ideal setup for quantifying and spatially mapping H-concentrations in various materials. The layout of the experimental setup is given in Figure 4. The FP5-Cave is roughly located 7 meters downstream of the 1L target and is 4 meters long. Starting from the high intensity moderator of the 1L target, neutrons are collimated down to a 3 cm beam spot with what is called the D-Collimation before entering the FP5-Cave. Once inside the cave a neutron is transmitted through a Tantalum foil to produce calibration dips in the transmission spectrum. Further downstream of the Ta calibration sample is a set of scrapping collimations meant to reduce background before the neutron beam impinges upon the sample. The sample is placed roughly 11 meters from the moderator of the 1L target. Directly downstream of the sample is the MCP-Timepix detector. This is a custom-designed pixilated neutron time-of-flight (TOF) imaging detector consisting of two chevron stacked microchannel plates (MCP) placed upstream of four Timepix application specific integrated circuits (ASICs) arranged in a 2x2 pattern. Utilizing a simultaneous readout of each Timepix chip, high frame rates of approximately 3000 frames per neutron pulse can be achieved. Previous work in determining low H-concentrations in zirconium alloys used destructive techniques to characterize hydrogen distributions in a sub set of the measured samples. These

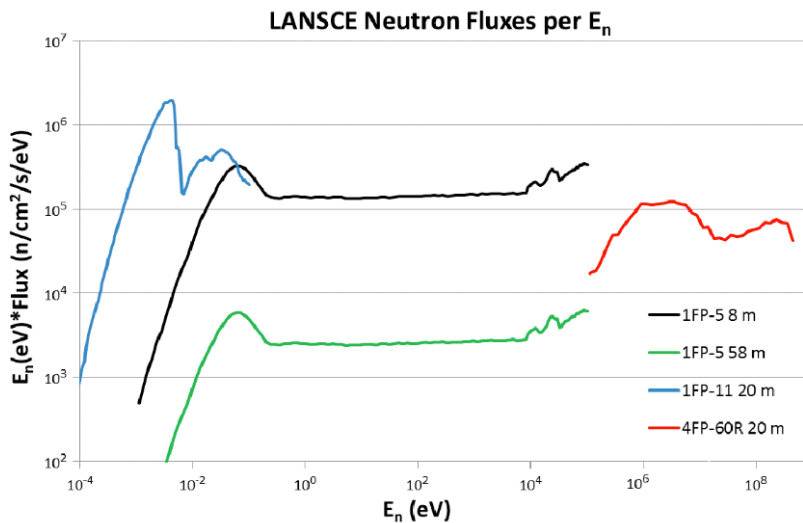


Figure 3. Plot taken from [Ref. 5]. The neutron energy spectra from the 1L target at the Lujan Center for flight path 5 (1FP-05) at 8 m (black) and 58 m (green), along with flight path 11 (1FP-11) at 20 m in blue. Additionally, a fast neutron spectrum for Flight path 60 right (4FP-60R) at 20 m, another neutron imaging beam line at the WNR, is included.

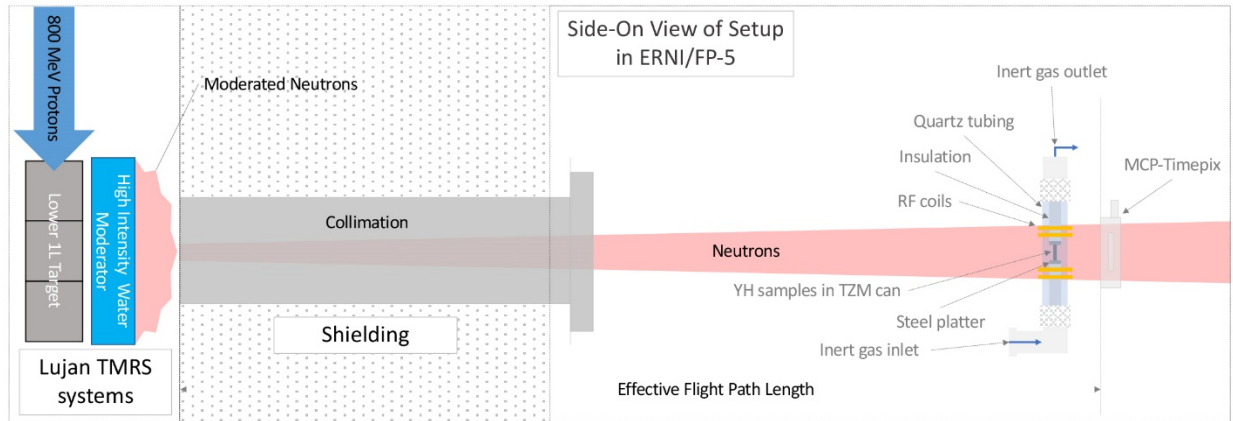


Figure 4. Setup for neutron radiography measurements on FP5. The sample and detector were placed roughly 11 meters downstream of the 1L target moderator. Additionally, ^3He detectors were deployed to observe neutron scattering and diffraction but results have not been analyzed and therefore are not reported here. Here neutron radiography was used to visualize potential hydrogen redistribution in yttrium hydride samples heated to up to $\sim 900^\circ\text{C}$ using a custom-built RF furnace.

results would then be used as a calibration for the rest of the sample group. For the FP5 measurements during the 2019 LANSCE beam cycle, instead of destroying a sub set of the samples, dedicated calibration samples were fabricated using high-purity aluminum housing and de-ionized water. A total of five calibration samples of water were fabricated with the following thicknesses: 100 μm , 250 μm , 500 μm , 1 mm, and 5 mm. The area of each calibration sample was a 5 cm by 5 cm square. Having well defined, highly polished aluminum cavities filled with water allowed for an accurate calibration of neutron attenuation vs H-concentration on a pixel-by-pixel basis without interference from the structural material holding the water (see Figure 5). This calibration could in theory be applied to other samples, such as YH_{2-x} to extract H-concentrations at each pixel. Each calibration sample was placed off-center (beam right) of the MCP-Timepix detector in order to leave a certain area open in the detector field of view. This “open beam” area was used to normalize each image stack based on its exposure to the neutron beam.

Next H-concentration measurements were performed using YH_{2-x} samples at room temperature/ambient conditions. The goal was to quantify hydrogen in four different YH_{2-x} samples with varying stoichiometry. The samples were sintered pellets with the following stoichiometries: $\text{YH}_{1.2}$, $\text{YH}_{1.6}$, and two $\text{YH}_{1.9}$. For these measurements, samples were paired

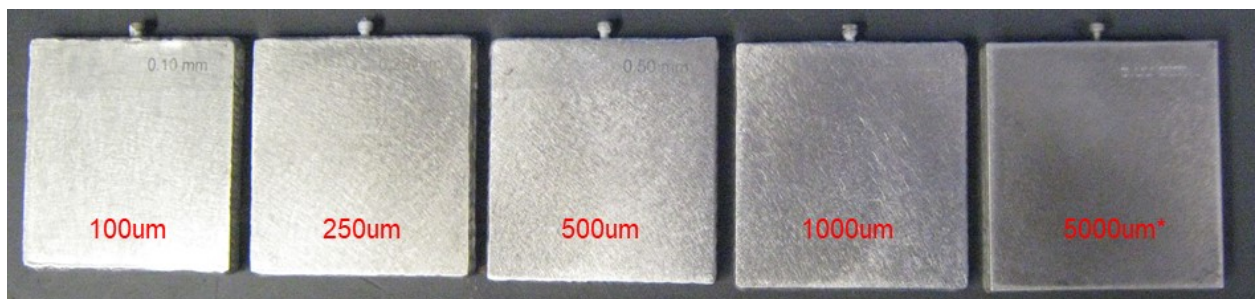


Figure 5. High purity water samples were used to calibrate attenuation coefficients. Using high purity H_2O in polished aluminum containers allows for uniform sample thicknesses and stoichiometries, which in turn reduce uncertainties in calibration.

together and place inside a vacuum sealed titanium-zirconium-molybdenum (TZM) can [32]. The first can contained a $\text{YH}_{1.2}$ and $\text{YH}_{1.9}$ sample, and the second can contained the other $\text{YH}_{1.9}$ sample along with a $\text{YH}_{1.6}$ sample. Results from these measurements are shown in Figure 6. The images to the left show background subtracted neutron counts (summed over all neutron energies) for the $\text{YH}_{1.6}$ and $\text{YH}_{1.9}$ samples (stacked on top of each other) and the 500 μm thick calibration sample. The red box in each image shows the region over which these neutron counts, as a function of energy, are averaged spatially and average neutron transmission as a function of neutron energy are then plotted in the right of Figure 6. The red line shows attenuation values for the $\text{YH}_{1.9}$ sample and the blue lines show attenuation values for the same region of pixels with the varying calibration samples.

3.1.2 Neutron Diffraction Experiments

Yttrium hydride powders with compositions $\text{YH}_{1.48}$, $\text{YH}_{1.81}$, and $\text{YH}_{1.92}$ were prepared following procedures described in Ref. 33, ground into powders and loaded into 6 mm diameter vanadium cans. Vanadium cans were chosen as vanadium has a negligible contribution to the neutron diffraction signal. Neutron diffraction data was collected on the high pressure/preferred orientation (HIPPO) neutron time-of-flight diffractometer at the 800 MeV proton accelerator-driven short-pulsed neutron spallation source at LANSCE. With HIPPO, neutrons were detected by 1,200 He $\frac{1}{2}$ inch detector tubes arranged on 45 detector panels on five detector rings with nominal diffraction angles of 40, 60, 90, 120, and 140°, covering 22.4% of 4π around the sample. Samples were loaded in a vacuum furnace with vanadium heating elements and heat shields, operating at a vacuum of $\sim 10^{-4}$ Pa. The furnace was controlled with a type-K thermocouple approximately 10 cm above the sample position in the ~ 15 cm tall hot zone. A second type K thermocouples served as an over temperature interlock and readout from both thermocouples were recorded. The sample position in HIPPO is ~ 8.9 m from the high flux/medium resolution ambient temperature water moderator. Data were collected with a 10mm diameter beam collimation for, at each temperature dwell point, the equivalent of nine times twenty minutes at

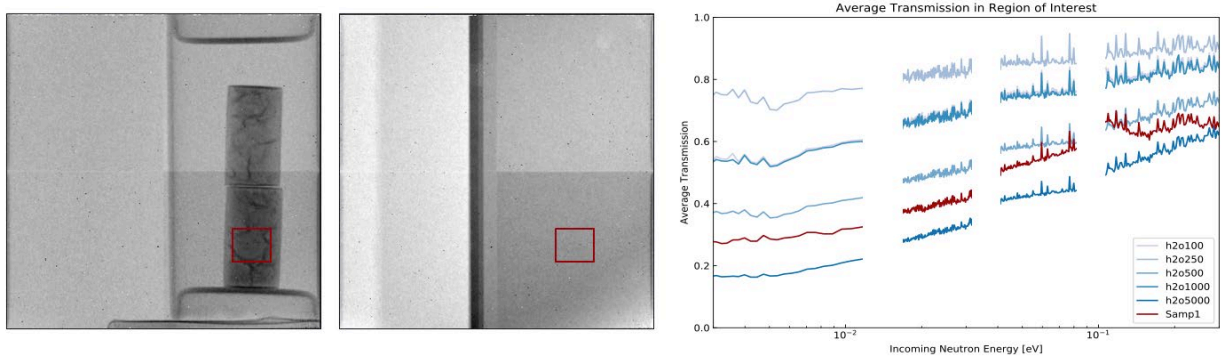


Figure 6. Preliminary results from ambient condition measurements. The two most left images show the Summed and flatten image stack of the $\text{YH}_{1.6}$ and $\text{YH}_{1.9}$ samples and the 500 μm thick calibration sample. The plot of the right shows averaged transmission spectra over a given region of interest (red box) for the $\text{YH}_{1.9}$ sample, along with all the water calibration samples.

a proton beam current of 100 μA , thus ensuring that each sample has received about the same amount of incident neutrons despite fluctuations of the proton beam current. The twenty minute long runs allow characterization of possible kinetic effects during holding, however, for the analysis presented here, all runs were integrated into one single datasets to improve counting statistics.

The data were analysed with the Rietveld method using the General Structure Analysis System (GSAS) driven by scripts developed in `gsaslanguage`, ensuring that each sample at each temperature was analysed with the same refinement approach. The initial structure for YH_2 used for the refinement was the one reported for room temperature by Khatamian et al. (space group $Fm\bar{3}m$, $a = 5.197 \text{ \AA}$) with both tetrahedral and octahedral sites defined. Yttrium with space group $P6_3/mmc$ and lattice parameters of $a = 3.6474 \text{ \AA}$ and $c = 5.7306 \text{ \AA}$ was used for the starting structure of metallic $\alpha\text{-Y}$. The starting site occupations for the fit were 0.95 and 0 for the tetrahedral and octahedral sites, respectively, and the thermal motion parameters U_{iso} were constrained to be identical for both H sites but independent for all other atoms (Y atoms in YH_2 and $\alpha\text{-Y}$). All thermal motion parameters started at a value of 0.01 \AA^2 . Diffraction data from the 140° , 120° , 90° , and 60° detector banks were refined simultaneously, excluding the lower resolution 40° data. To accommodate for the strong background from the incoherent scattering of hydrogen, 12 parameters of the GSAS background function #1 were refined for each histogram. Leaving the YH_2 lattice parameter fixed at a value of 5.2077 \AA (determined from ambient condition datasets with Cu as an internal standard), the time-of-flight to d-spacing conversion factors were refined for all histograms, essentially recalibrating the sample position for each sample. Lattice parameters of YH_2 and $\alpha\text{-Y}$, site occupation factors of tetrahedral and octahedral sites (without constraining the overall composition), thermal motion parameters U_{iso} for all atoms, one absorption parameter per histogram to accommodate for the beam attenuation from the incoherent scattering cross-section of the hydrogen atoms, and peak width parameters σ_1 of the GSAS peak profile function #1 were refined in this sequence, roughly following the contribution of each parameter to the difference curve. After the ambient condition refinement, the absorption parameters and diffractometer constants were fixed and the ambient condition refinement was used as starting point for all other refinements with prescribed changes of the starting values for lattice parameters for temperatures above 700°C . An example of the refinement is shown in Figure 7.

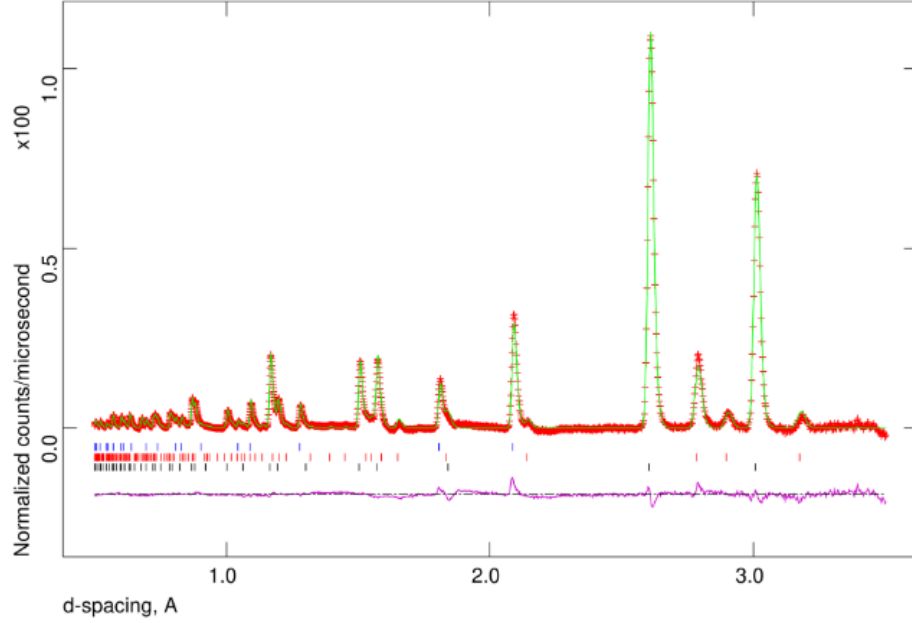


Figure 7. Example of a Rietveld refinement for the YH_{1.48} sample, data from the 90° detector panel normalized by the incident intensity are shown as red crosses with the Rietveld fit as a green line. The difference curve is shown below. The background is subtracted for clarity. Rows of tickmarks indicate calculated reflections positions for δ -YH₂ (bottom row), α -Y (center row), and the Cu internal standard (top row).

3.2 Hydrogen Diffusion Measurements

3.2.1 Spatially mapped hydrogen concentrations at different temperatures

Additional to the measurements performed at ambient conditions, two sets of neutron radiography measurements at higher temperatures were performed. The setup for neutron radiography on FP5 is shown in Figure 4 [8]. Pulsed neutrons stream out of the high intensity moderator of the target-reflector-moderator system (TRMS) and down the collimation of FP5 [9]. Located ~10 meters from the moderator are the yttrium hydride samples in front of a MCP-Timepix detector. First, ERNI measurements were performed on YH samples that were heated to elevated temperatures using a Carbolite-Gero tube furnace. These measurements were performed on FP5 over the period of two days, and in total, 6 ERNI measurements were performed over the following temperature profile: 33 °C, 200 °C, 400 °C, 540 °C, 770 °C, and finally 50 °C. The setup for the elevated measurements was similar to the ambient measurements and is shown in Figure 8.



Figure 8. Image of setup for elevated temperature measurements taking with YH_{2-x} samples on FP5. This setup was very similar to the ambient condition measurements, with just the addition of the Carbolite-Gero tube furnace to heat YH samples up to $\sim 800^\circ\text{C}$.

The TZM container discussed in Section 3.1.1 with the YH1.6 and YH1.9 samples was selected for these elevated temperature measurements. The samples were suspended inside the furnace using molybdenum wire. Unfortunately, while installing the samples into the tube furnace one of the samples fell over and partially obscures the other samples, making it extremely difficult to figure out which sample has which stoichiometry. Nevertheless, regions-of-interest were found for each sample such that there was no interference from the other. These ROIs are shown in the left image of Figure 9. With these ROIs and a selected region for normalization, neutron counts observed in the MCP-Timepix could be directly compared across the range of temperatures recorded. It should be noted here that any “open beam” measurements needed for actual transmission could not be taken as there was a slight amount of movement with the furnace and the sample. Therefore, only raw neutron counts can be only relatively compared to each other to get any sort of meaning for results. The right plot shows the resulting summed neutron counts within both regions of interest over the range of temperatures recorded.

Next, a measurement was performed with the two different yttrium hydride samples of stoichiometries of 1.15 (~ 1.2) and 1.63 (~ 1.6) discussed in Section 3.1.1 stacked on top of each other in a titanium-zirconium-molybdenum (TZM) can. The samples were placed inside a custom-built Radiofrequency (RF) furnace capable of reaching temperatures up to $\sim 1000^\circ\text{C}$. We measured temperatures within the furnace continuously with K-type thermocouples placed above and below the sample, and a cover gas of Argon continuously flowed throughout the main tube to prevent oxidation of the sample container (see Figure 4). With the RF furnace, the samples were assessed through the following temperature profile of intermixed heating and cooling to understand cycling effects: 650°C , 750°C , 780°C , 800°C , 820°C , 840°C , 860°C , 880°C , 895°C , 750°C , 850°C , 825°C , 800°C , 775°C , 750°C , and finally 700°C . Six 30-minute exposures were taken at each temperature. These sample images, plus an image without the sample were then used to obtain transmission and attenuation images at each temperature from which hydrogen distributions can be visualized within the yttrium hydride samples. Selected resultant attenuation images of the yttrium hydride samples are shown in Figure 10 for several temperatures during heating and cooling process. One of the key observations was that the lower sample appeared to accumulate more hydrogen throughout the cooling process of the

measurement, though the actual spatial temperature profile (top to bottom) of the pellets within the sample container was not measured or well understood. The exact cause of this observation is not known, but experimentally, the determination of the temperature profiles in the sample is complicated by the requirement of the sample pellets being enclosed in the container materials. Enclosing the sample simulates the moderator in a reactor and without this enclosure the hydrogen would likely leave the system instead of redistributing within the pellets. This type of setup is different from previous high temperature neutron radiography studies where the sample was exposed to a controlled atmosphere to study e.g. hydriding of zirconium in a steam atmosphere, providing the ability to have thermocouples [34,35]. Further information on temperature and stoichiometric distributions in the samples is needed to make more informed conclusions, and analysis is still on-going.

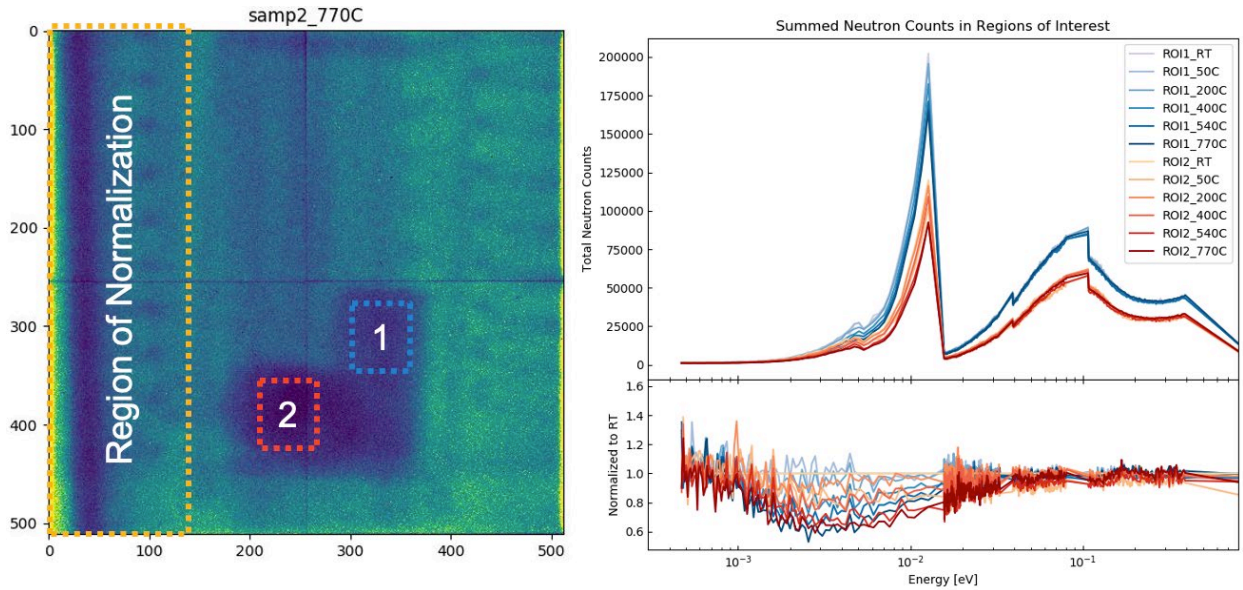


Figure 9. (Left) Summed and flattened image stack of the 770 C measurements with the $YH_{1.6}$ and $YH_{1.9}$ samples. Regions of interest were selected for each sample in order to compare neutron counts across the full range of temperatures. (Right) Average neutron counts as a function of neutron energy within each of the regions of interest.

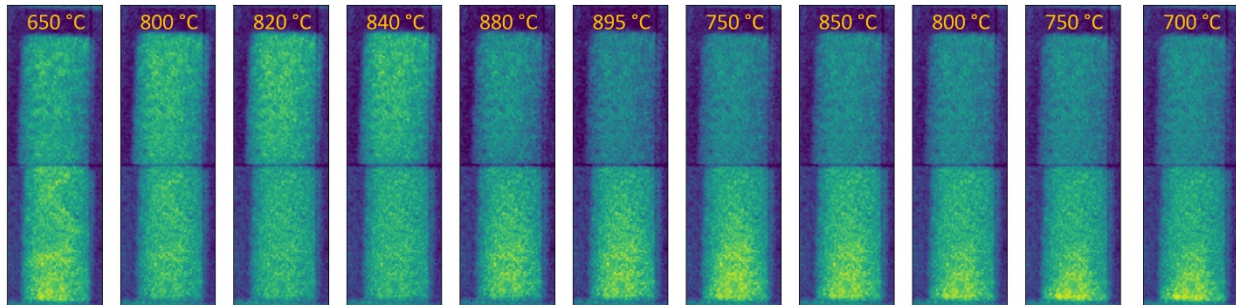


Figure 10. Attenuation images with highly adjusted contrast of YH_{2-x} samples taken at several temperatures using neutron radiography on FP5. Yellow indicates a higher hydrogen concentration than the blue.

3.2.2 Diffusivity and Thermal Conductivity as a function of stoichiometry

Thermal conductivity was calculated using results of the diffraction measurements [33]. Observation of hydrogen movement such as that shown in Figure 10 can lead to determining diffusivity of yttrium hydride samples, but more work is needed to calibrate the hydrogen concentrations and understand the time frame of diffusion first.

3.3 Characterize point defects and other parameters

Data collected from the measurements discussed in Section 3.1 were used to generate cross sections for predictive calculations of hydrogen performance through Density Functional Theory and other codes as described below.

3.3.1 Methods for Modeling Hydrogen Materials

As discussed in Section 2.2, first principles quantum mechanical simulations were performed using the density functional theory (DFT) code VASP. Generalized gradient approximation (GGA) with Perdew-Burke-Ernzerhof (PBE)-generated projected augmented wave (PAW) potentials were used to describe the exchange-energy correlational functional in a supercell consisting of a $2 \times 2 \times 2$ extension of the fluorite unit cell. The sub-stoichiometric YH_{2-x} structure can be modeled using a random distribution of sub-stoichiometric defects (of which H vacancies were found to be the most stable). However, as DFT methods accompany relatively small supercell size, for this reason it is not entirely possible to generate a truly random distribution of defects. Therefore, the special-quasirandom-structure (SQS) Monte-Carlo method implemented in the Alloy Theoretic Automated Toolkit (ATAT) was employed in our study to mimic the correlation functions of an infinite random system. This ensures that the configuration space of the finite supercell approximates that of an ideal random structure. Elastic properties of the yttrium hydride system were generated using these structures for various compositions. The Phonopy code was used to create a series of finite displacement structures from the energy minimized SQS structures for each sub-stoichiometric yttrium hydride composition. The interatomic forces for these displaced structures were then calculated using VASP to determine the phonon density of states. It should be noted that the varying composition of yttrium hydride is modeled using a single-phase structure (YH_{2-x}), which is true for concentrations $1.3 \leq \text{H}/\text{Y} \leq 2$ at temperatures above 600 °C. For $\delta\text{-YH}_{2-x}$, a planewave basis set kinetic energy cutoff of 500 eV were used to expand the wave functions for these structures. Monkhorst-pack mesh of $5 \times 5 \times 5$ was sampled by converging the system energy to 1 meV per atom. The electronic loop and ionic loop were converged within 1×10^{-6} eV and 1×10^{-5} eV, respectively, for the system energy minimization. To account for the lattice expansion, the quasi-harmonic approximation (QHA) was utilized using the Phonopy code. Perfect $\delta\text{-YH}_2$ supercells were used to create nine supercells with distinct volumes. Using these different volumes, the phonon density of states were determined through the finite displacement method, as described earlier. Once the phonon density of states was produced for all volumes, QHA was utilized to generate the thermal expansion parameters. NJOY2016 was used to generate the thermal scattering laws for sub-stoichiometric yttrium hydride.

3.3.2 Evaluated atomic scale results on point defect behavior in YH_x as a function of stoichiometry

The DFT-QHA simulations and neutron diffraction experiments produced thermal lattice strains for yttrium dihydride as shown in Figure 11a. There is excellent agreement between both data. The thermal displacement parameters (Figure 11b) are an indicator of how the atoms are displaced due to phonons in a potential well. The results for the non-stoichiometric compositions show the impact of point defect behavior (specifically H vacancies) on thermal expansion. There is excellent agreement between both modeling and experiments up to ~ 1000 K temperatures after which the high temperature results in the H atoms being displaced from their tetrahedral sites, which causes the U_{iso} to rise significantly in the experimental data. This is likely due to a transition of the material into a so-called superionic state, which is not modeled by DFT by subject to further investigations modeling the deviation from a perfect fluorite crystal structure using maximum-entropy methods for the diffraction data analysis. Additional modeling work should use molecular dynamics (MD) to investigate the onset of the superionic transition and its impact on material properties. The lack of a suitable empirical potential prohibited the use of classical MD in this study but DFT-MD, which is more computationally expensive, could be employed in the future. The agreement between modeling and experimental results provide great confidence in the thermomechanical, and nuclear properties generated using DFT for temperatures below the superionic transition [36-41].

DFT analysis was extended to account for mechanical properties as a function of sub-stoichiometry (Figure 12a). This is important for the structural analysis required for the yttrium hydride moderated microreactors. The elastic properties show that the material becomes less stiff as one decreases the hydrogen concentration. After generating the phonon density of states using VASP/PHONOPY codes, the thermal scattering laws for sub-stoichiometric yttrium hydride were generated using NJOY as a function of stoichiometry and temperature (Figure 12b) and can be used as input for the MCNP transport code. In particular, these evaluations were fed into high-

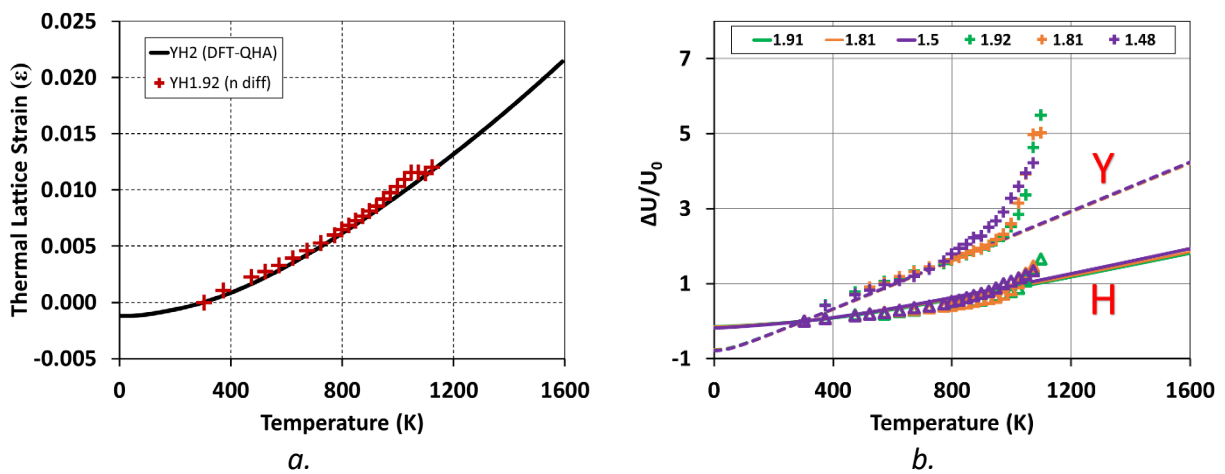


Figure 11. (a) DFT-QHA (YH_2) and neutron diffraction ($\text{YH}_{1.92}$) comparison of the thermal lattice strain. (b) Comparison of DFT and neutron diffraction atomic displacement parameters. Markers represent neutron diffraction data, whereas lines represent DFT data. The legend provides H/Y ratios.

fidelity neutronics modeling, including reactivity safety analysis, for yttrium hydride moderated microreactors as discussed later in this document. It was found that as H/Y decreases, the hydrogen incoherent cross-section increases between energies 10^{-3} to 10^{-1} eV due to the new phonon modes activated in the optical range from crystal asymmetry. However, at higher temperatures (>1500 K), the inelastic component saturates for all energies. This suggests that temperatures above 1500 K overrides the phonon modes activated due to asymmetry, removing the stoichiometry dependency for the hydrogen σ_{in} cross-sections. This might be purely hypothetical since in the neutron diffraction experiments under vacuum the YH_2 disintegrated into metallic yttrium and hydrogen gas at $\sim 1100\text{K}$. While a different gas atmosphere may change the decomposition temperature, YH_2 is likely not stable at 1500K.

During assessing the neutron diffraction results and the comparison with DFT results, we discovered an anomaly with increasing temperatures which resulted in a discovery of the Bredig transition in the yttrium hydride crystal structure. A direct observation of the Bredig transition in a hydride system was made to the best of our knowledge for the first time using the neutron diffraction experiments. There could be several interpretations as to whether a true Bredig transition was seen, and therefore, for the remainder of the discussion, we defend our statement. Initially, a hypothesis can be made showing that this phenomenon is a result of hydrogen diffusion in the metal hydride system. Another possible explanation could also be that the hydrogen atoms are migrating from tetrahedral sites (t-sites) to octahedral sites (o-sites). However, this phenomenon could not explain why the t-site occupation factor decreases without any increase in the o-site occupation factor. The t-site occupation factor for $\text{YH}_{1.48}$ continues to decrease from 800 K to 1075 K (Figure 13b). Figure 13a shows that the $\text{YH}_{1.48}$ transitions from a two-phase to single-phase region between 800 K and 900 K, thus explaining the decrease in the

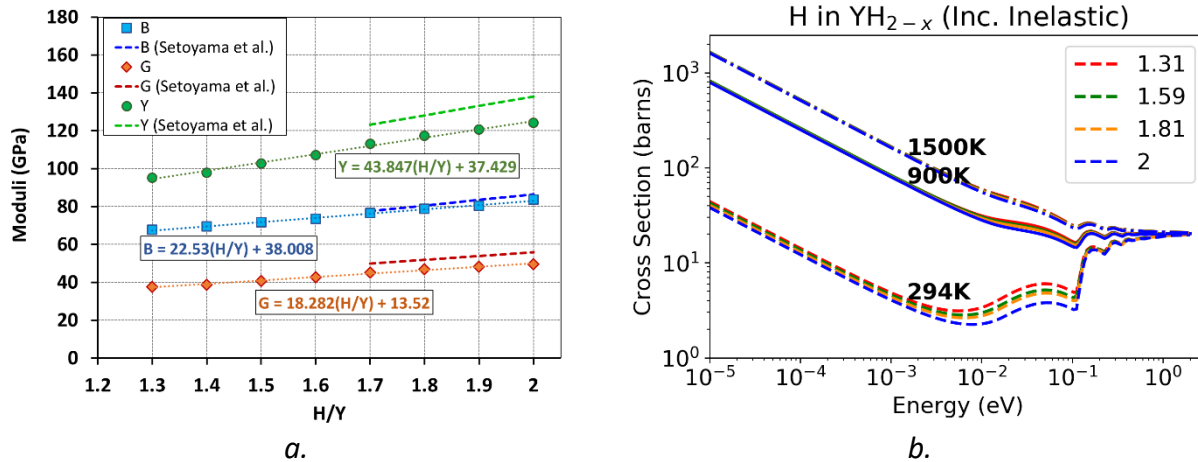


Figure 12. (a) Derived single-phase YH_{2-x} polycrystalline elastic properties from DFT, (b) Thermal scattering evaluations for stoichiometry dependent yttrium hydride (x in $\delta\text{-YH}_{2-x}$).

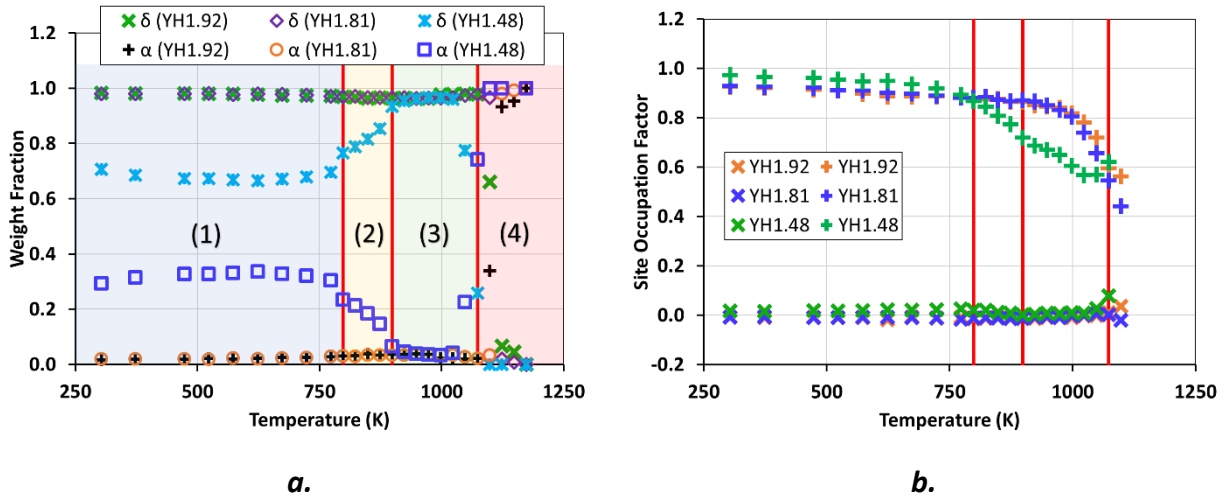


Figure 13. Neutron diffraction analysis of (a.) weight fraction of α -Y and δ -YH_{2-x} in yttrium hydride samples, and (b.) site occupation factor of hydrogen in tetrahedral sites (plus symbol) and octahedral sites (cross symbol). The four regions in (a.) represent (1) two-phase region, (2) transition to single-phase region, (3) Bredig transition, and (4) H dissociation for YH_{1.48}.

hydrogen t-site occupancy without any increase in o-site occupancy. However, between 900 K and 1000 K, there is no changes in the yttrium hydride phases, but the t-site occupancy continues to decrease. This is true for the other two stoichiometries YH_{1.81} and YH_{1.92} in that these two compositions did not go through a substantial decrease in the t-site occupancies for temperature below 900 K.

3.3.3 Developed an approach for experimentally obtaining thermal scattering cross sections with differential die away techniques.

We held a workshop to discuss differential-die away techniques for measuring the thermal scattering cross section of yttrium hydride. Participants included: Ben Forget at MIT, Gunter Muhrer at the European Spallation Neutron Source, Mike Zerkle from Bettis Labs, and Bob Little, Jeremy Conlin, Theresa Cutler, and Holly Trelue from Los Alamos. A technique for measuring thermal scattering cross sections using different sizes of yttrium hydride samples and results from differential die-away measurements in a well counter was discussed [42]. However, these measurements were not within the scope of this project because different techniques for developing thermal scattering laws using results of the LANSCE measurements were implemented instead. Such measurements with a well counter and disks of sizes one to two inches in diameter are feasible in the future though.

3.4 Developed an automated multi-physics framework for advanced reactor analysis with the Monte Carlo N-particle (MCNP) transport code -linked to the thermal mechanical analysis code ABAQUS

Using data obtained from measurements and/or density function theory and processed NJOY cross section sets, the performance of a moderator material can be assessed more accurately with the MCNP code. To assist in such an evaluation, enhancements were made to the MCNP functionality. These enhancements included the ability to input more detailed information by small portions of a geometry (element sets) and the capability to produce data needed by

deterministic reactor modeling codes for multi-physics calculations. In addition, an automated framework for some of the code linkages was created. Finally, results of the integrated experimental and modeling efforts were combined for a sample microreactor problem to demonstrate performance in the system using knowledge gained through this project.

3.4.1 The MCNP code was modified to input densities and temperatures individually for each element set within an ABAQUS unstructured mesh model.

The MCNP code is a general-purpose, continuous-energy, generalized-3D-geometry, time-dependent, particle transport code. MCNP geometries are organized into cells bounded by surfaces. This type of MCNP geometry is known as a constructive solid geometry (CSG). To perform MCNP simulations, geometries (cells and surfaces) and material properties (densities, temperatures, etc.) are defined in MCNP input files. MCNP version 6 (also known as MCNP6) has the capability to perform calculations on hybrid geometries that consist of unstructured mesh (UM) geometry representations embedded as universes using the legacy CSG. Two input file types are required for MCNP UM calculations: MCNP input and mesh geometry files. Currently, the MCNP code can only read and process the mesh geometry formatted as an Abaqus input file.

An Abaqus UM model is based on part and assembly definitions where each part can be used (instanced) one or more times to form an assembly of part instances. A part contains elements that are organized into sets, known as element sets or elset. The MCNP code uses the element set concept to assign material numbers to parts. The elset definitions in the part-level and the instance definitions in the assembly-level are used to create pseudo-cells in the MCNP input file. The material properties such as densities and temperatures are assigned to the MCNP pseudo-cells. The modified MCNP code was modified to process an Abaqus input file where each part may be separated into several element sets based on densities or temperatures [43]. These MCNP code changes will be released to public in the MCNP 6.3 version. In addition, we have developed a Python code-based framework used to (i) extract an unstructured mesh geometry and then write an MCNP input file [44] and (ii) process an MCNP output file and then write an Abaqus input file [45].

The MCNP code reads and processes Abaqus input files that make use of part and assembly definitions. An Abaqus UM model is created by defining parts and then assembling instances of each part. Each part can be used (instanced) one or more times where each part instance has its own position within the assembly. Only one assembly can be defined in a model. A component defined within a part, instance, or the assembly is local to that part, instance, or the assembly. A part definition must appear outside the assembly definition. Multiple parts can be defined in a model and each part must have a unique name. An instance definition must appear within the assembly definition where each instance must have a unique name and refer to a part name. Data lines may be used to position the instance within the assembly. These positioning data lines include a translation and rotation for the instance relative to the origin of the assembly coordinate system. Other components must be categorized and fall within the proper level: part, assembly, instance, or model. Material definitions are model-level data. The components in the part-level required by the MCNP codes include node, element, and element sets.

MCNP and Abaqus input files required for MCNP UM simulations must be related, i.e. pseudo-cells in the MCNP input file must be constructed from mesh information defined in the Abaqus input file. Thus, we developed a Python code to write a MCNP UM input file. The intent of this code is to make easier for the users to set up the files. In addition, we developed the Python code for post-processing an elemental edit output. These Python codes were approved for public release and users can download from the MCNP website.

3.4.2 New Multigroup Tally Options in the MCNP6 Code

Additionally, several new multigroup (MG) special treatment tally options were implemented, tested, and should be in the next release of the MCNP6 code, version 6.3. These new special tally treatment options were developed to facilitate the production of transport parameters that characterize the transmission and scatter of neutrons within a material region. In a MG form, the cross sections can be used for more computationally efficient Monte Carlo or deterministic transport calculations as well as for diffusion, reactor kinetics and other multi-physics simulations.

Summary of new MG tally options

Four new tally special treatment options on the MCNP FT card, shown in Table 1, have been added to calculate MG cross sections, angular distributions and fission spectra.

First, the *mgc* option computes 10 different neutron incident energy-grouped quantities based on a user-specified energy bin structure. The 10 quantities computed and corresponding units are shown in Table 2.

Next, the *spm* and *lcs* options compute MG differential neutron scattering quantities in two different forms. For *spm*, the scattering matrices are tallied in three dimensions: incident energy by outgoing energy by cosine of the scatter angle, for a user-defined cosine binning structure. For *lcs*, the scattering matrices are also computed in three dimensions: incident energy by outgoing energy by Legendre polynomial order, which is also a user-specified quantity.

Finally, the *fns* option computes the total/prompt and delayed fission neutron spectra. A user can either supply a time bin structure to separate prompt and delayed fission neutrons, or the default ENDF/B time bin structure is setup to separate the 6 primary delayed fission precursor families. The final tallied spectra for each time bin or prompt and delayed fission groups are computed in two dimensions: incident energy by outgoing energy.

Table 1. New MG Tally Options

FT Card Option	Description
<i>MGC</i>	Flux weighted multigroup cross sections
<i>SPM</i>	Collision exit energy-angle scatter probability matrices
<i>LCS</i>	Legendre coefficients for scatter reactions
<i>FNS</i>	Induced fission neutron spectra

Table 2. MGC Quantities Computed

MGC Quantity	Units
<i>Flux</i>	neutrons/cm ² ·s
<i>Inverse velocity</i>	shakes/cm
<i>Total cross section</i>	barns
<i>Capture cross section</i>	barns
<i>Fission cross section</i>	barns
<i>Total/prompt fission production cross section</i>	barns
<i>Delayed fission production cross section</i>	barns
<i>Fission heat production cross section</i>	MeV-barns
<i>Absorption (capture + fission) cross section</i>	barns
<i>Scatter (total - absorption) cross section</i>	barns

Verification of new MG tally options

Several test problems were studied to verify the implementation of the new MG tally options [46]. Very briefly, the cross sections, angular distributions and fission spectra were compared to both continuous-energy nuclear data as well as to MG data computed by the nuclear data processing code NJOY2016. Figure 14 shows various examples of the cross sections, angular

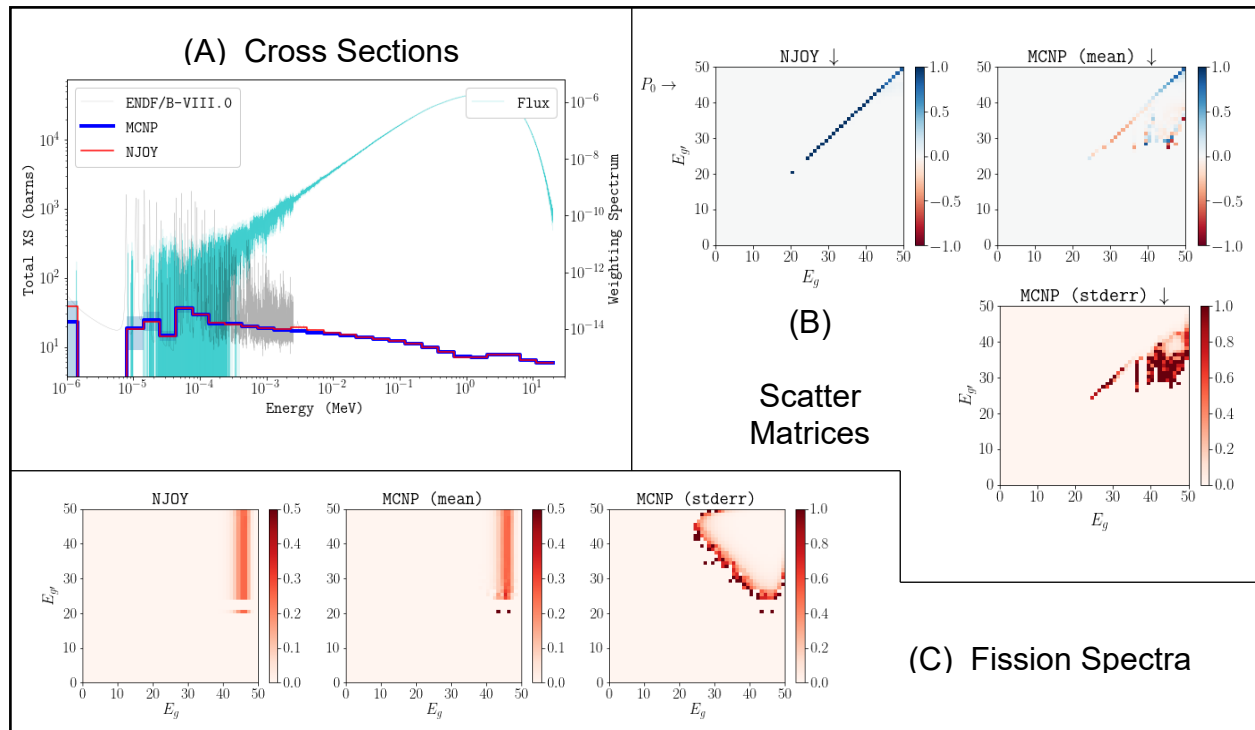


Figure 14. MG verification comparisons to NJOY-computed MG data. The upper left panel (A) shows a total cross section and weighting flux spectrum, the upper right panel (B) shows the P_0 scattering matrix, and the bottom panel (C) shows the prompt fission neutron spectrum in matrix form.

scattering distributions, and fission spectra compared to continuous-energy and NJOY results. Through the verification efforts, it is concluded that the MG tally options are implemented properly. Some additional future work should be focused on computing more multigroup cross sections, e.g. photon production and reaction cross sections, and in applying variance reduction methods to these tallies for improved efficiency in the convergence of the statistical uncertainties of these MG tally quantities [47].

3.4.3 An ABAQUS-MCNP framework plus a code linking between the MCNP code and the kinetics code in the DireWolf tool suite.

Finally, a new automated framework was developed to ease the process of linking MCNP and ABAQUS for small reactor multi-physics calculations. In particular, the Python code `um_pre_op.py` was used to write an MCNP input file and to automate the flow of information between the codes [48]. Note that the `um_pre_op.py` code was later modified for use in other applications at LANL [44]. In addition to the `um_pre_op.py` code, other python codes were developed to automate an MCNP and Abaqus multiphysics simulation and this multi-physics calculation framework is called MARM (MCNP-Abaqus based Reactor Multiphysics). A flow diagram of MARM is shown in Figure 15 and the detailed Python algorithm is shown in Appendix A. A three dimensional representation of how element sets are generated is given in Figure 16.

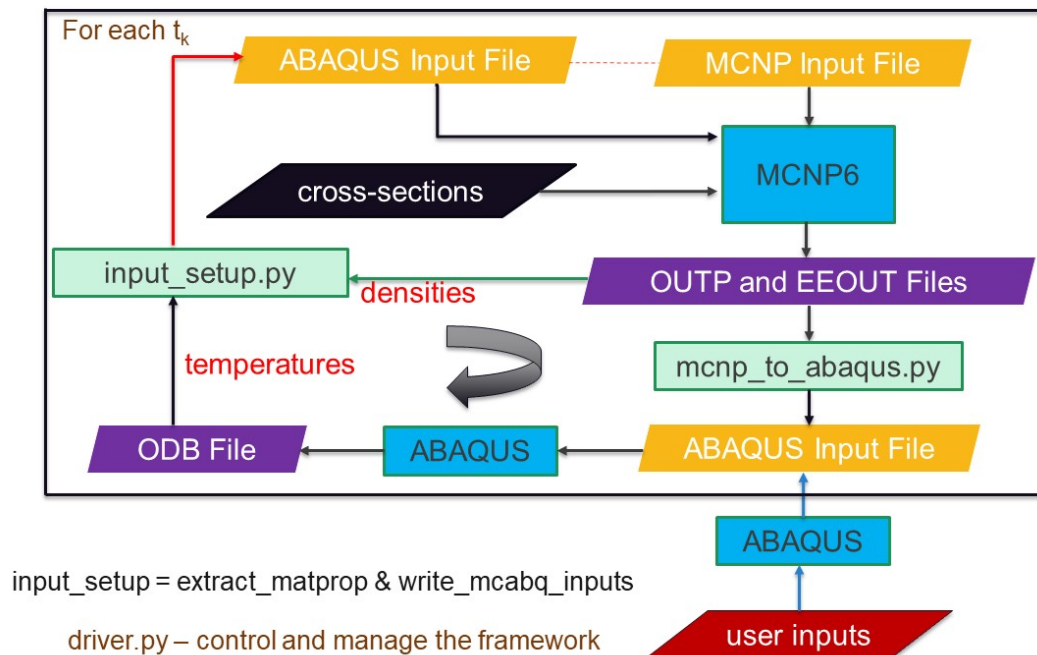


Figure 15. Flow Diagram for MARM Framework

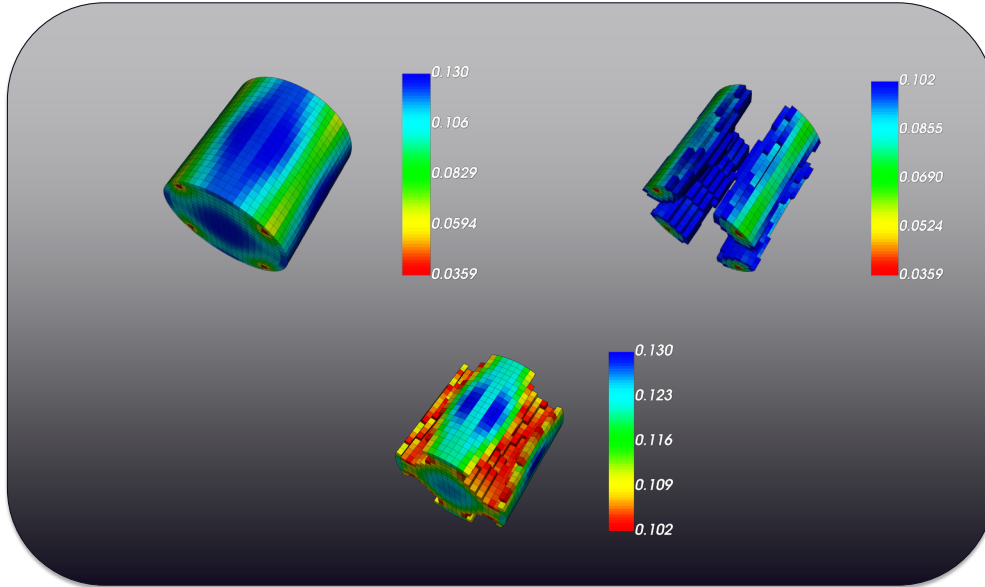


Figure 16. Three-dimensional representation of selective element set generation

3.4.4 Evaluation of a moderated microreactor system

To demonstrate the effect of varying hydrogen concentrations, we used the new cross sections described in Section 3.3 and representative distributions in a MCNP model of a microreactor infinitely-reflected multi-unit cell (see Figure 17). Moderating material exists both in the form of the graphite structural monolith that contains the fuel rods, sodium-filled heat pipes, and yttrium hydride [49]. By separating the cylindrical moderator into three regions of equal volumes, MCNP calculations were performed using the new cross sections developed in this project both with a homogeneous stoichiometry for YH_x of $x=1.8$, for stoichiometries of 2.0/1.8/1.6 and 1.6/1.8/2.0 in the three zones respectively, and simplified distributions as seen at the end of the measurements described in Section 3.2 and shown to the right in Figure 17. We retained the same total hydrogen concentration in all calculations. As shown in Table 3, we observed small

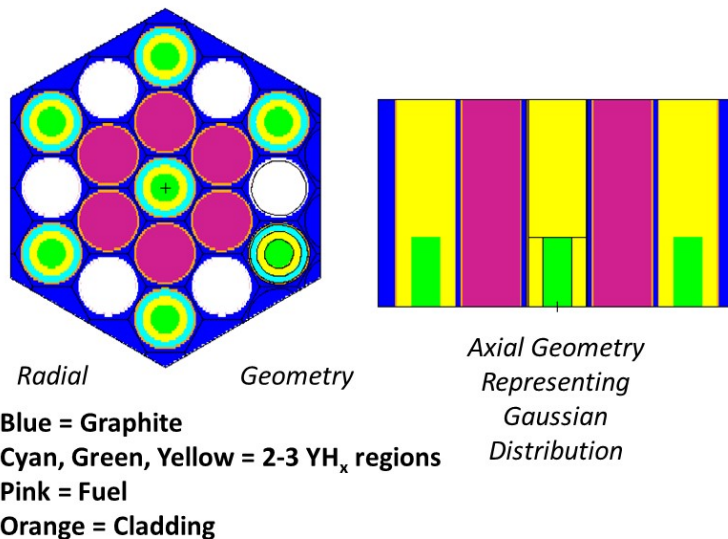


Figure 17. Geometry of an example of a microreactor hex block with one moderator rod in the middle, 6 fuel rods in the inner row, and 12 moderator rods in the outer row.

Table 3. Effect of Hydrogen Distribution on k_{eff} (1 pcm = change in k_{eff} of $1\text{e-}5$)

Distribution	Difference in k_{eff} +/- 0.00016
Average ($\text{YH}_{1.8}$)	-
$\text{YH}_{2.0/1.8/1.6}$	231 pcm
$\text{YH}_{1.6/1.8/2.0}$ (inner to outer radial regions)	-147 pcm
Gaussian-like distribution with higher stoichiometry in center	51 pcm
Gaussian-like distribution with lower stoichiometry in center	2 pcm

differences in k_{eff} (neutron multiplication) amongst the various cases. Note that changes on the order of thousands of pcm result from other geometric and operational variations, so the values in Table 3 are fairly insignificant.

4.0 Conclusions

In summary, we have significantly advanced our ability to predict performance of moderator material through both experimental and theoretical research through subject matter experts in various fields working together. The capabilities developed through this project will be able to be applied to a wide range systems and applications for years to come. First, we observed the redistribution of hydrogen at temperatures above 800°C in yttrium hydride material.

Next, we developed a comprehensive framework for the prediction of the cross-sections of sub-stoichiometric YH_{2-x} for moderator applications and benchmarked it with experimental methods. The DFT predictions, ultimately used to predict the high temperature cross-sections, were compared with results for the stoichiometric compound and parameters derived from the stoichiometry and temperature dependent DFT model, such as lattice parameters and atomic displacement parameters, were compared with results from high temperature neutron diffraction experiments. During this effort, indications that YH_2 transitions into a superionic state, the so called Bredig transition, were observed in the experiment. Several peer-reviewed publications resulted from this effort and with several more publications in progress.

In addition, we enhanced the MCNP code for reactor applications with materials such as moderators with significant modifications. Temperature and density information can now be passed from the finite element code Abaqus to the MCNP code on small geometric scales, and multi-group cross sections, scattering moments, and velocities can now be obtained from the MCNP code for larger multi-physics calculations such as thermal mechanical and transient evaluations with subsequent deterministic codes. The project advanced core infrastructure capabilities at the laboratory that will lead to new programs such as microreactors and/or uranium hydride characterization in the near future.

The work is transitioning to several different programs: 1) improvements to unstructured mesh simulation capabilities is being enhanced and tested through other LDRD DR projects, and 2) the ability to measure hydrogen redistribution is important for Microreactor applications, including both Department of Energy Advanced Research Projects Agency–Energy (ARPA-E) collaborations with industry and Department of Energy – Nuclear Energy Advanced Reactor Demonstration/Microreactor Programs.

References

1. Beck, R. L. & Mueller, W. M. Zirconium Hydrides and Hafnium Hydrides. *Metal Hydrides* 241–335 (1968).
2. Mueller, W. M., Blackledge, J. P. & Libowitz, G. G. *Metal Hydrides*. (Elsevier, 1968). doi:10.1016.
3. IAEA, 2018: Advances in Small Modular Reactor Technology Developments: A Supplement to: IAEA Advanced Reactors Information System (ARIS), 2018 Edition.
4. Chang, J. Table of Nuclides, KAERI (Korea Atomic Energy Research Institute).
5. O. R. Nelson, C. S. Vogel, F. J. Hunter, B. E. Watkins, S. A. Losko, S. A. Tremsin, P. N. Borges, E. T. Cutler, T. L. Dickman, A. M. Espy, C. D. Gautier, C. A. Madden, J. Majewski, W. M. Malone, R. D. Mayo, J. K. McClellan, S. D. Montgomery, M. S. Mosby, T. A. Nelson, J. K. Ramos, C. R. Schirato, K. Schroeder, A. S. Sevanto, L. A. Swift, K. L. Vo, E. T. Williamson, and M. N. Winch, “Neutron Imaging at LANSCE—From Cold to Ultrafast,” 2018.
6. A. Agrawal, Y. Kashyap, P. Sarkar, A. Behra, M. Shukla, R. Singh, A. Sinha, and J. Chakravartty, “Study of hydride blisters in Zr-alloy using neutron tomography,” *Journal of Nuclear Materials*, vol. 421, pp. 47–53, feb 2012.
7. N. L. Buitrago, J. R. Santisteban, A. Tartaglione, J. Marín, L. Barrow, M. R. Daymond, M. Schulz, M. Grosse, A. Tremsin, E. Lehmann, A. Kaestner, J. Kelleher, and S. Kabra, “Determination of very low concentrations of hydrogen in zirconium alloys by neutron imaging,” *Journal of Nuclear Materials*, vol. 503, pp. 98–109, 2018.
8. M. Grosse, E. Lehmann, P. Vontobel, and M. Steinbrueck, “Quantitative determination of absorbed hydrogen in oxidised zircaloy by means of neutron radiography,” *Nuclear Instruments and Methods in Physics Research Section A: Accelerators, Spectrometers, Detectors and Associated Equipment*, vol. 566, pp. 739–745, oct 2006.
9. M. Grosse, C. Roessger, J. Stuckert, M. Steinbrueck, A. Kaestner, N. Kardjilov, and B. Schillinger, “Neutron Imaging Investigations of the Secondary Hydriding of Nuclear Fuel Cladding Alloys during Loss of Coolant Accidents,” *Physics Procedia*, vol. 69, pp. 436–444, 2015.

10. M. K. Grosse, J. Stuckert, M. Steinbrück, A. P. Kaestner, and S. Hartmann, "Neutron Radiography and Tomography Investigations of the Secondary Hydriding of Zircaloy-4 during Simulated Loss of Coolant Nuclear Accidents," *Physics Procedia*, vol. 43, pp. 294–306, 2013.
11. M. Grosse, M. Van Den Berg, C. Goulet, E. Lehmann, and B. Schillinger, "In-situ neutron radiography investigations of hydrogen diffusion and absorption in zirconium alloys," *Nuclear Instruments and Methods in Physics Research, Section A: Accelerators, Spectrometers, Detectors and Associated Equipment*, vol. 651, no. 1, pp. 253–257, 2011.
12. R. Yasuda, M. Nakata, M. Matsubayashi, K. Harada, Y. Hatakeyama, and H. Amano, "Application of hydrogen analysis by neutron imaging plate method to Zircaloy cladding tubes," *Journal of Nuclear Materials*, vol. 320, pp. 223–230, aug 2003.
13. W. Gong, P. Trtik, S. Valance, and J. Bertsch, "Hydrogen diffusion under stress in Zircaloy: High-resolution neutron radiography and finite element modeling," *Journal of Nuclear Materials*, vol. 508, pp. 459–464, sep 2018.
14. S. Vogel, E. Ustundag, J. Hanan, V. Yuan, and M. Bourke, "In-situ investigation of the reduction of NiO by a neutron transmission method," *Materials Science and Engineering: A*, vol. 333, pp. 1–9, aug 2002.
15. Y. Su, K. Oikawa, S. Harjo, T. Shinohara, T. Kai, M. Harada, K. Hiroi, S. Zhang, J. D. Parker, H. Sato, Y. Shiota, Y. Kiyonagi, and Y. Tomota, "Time-of-flight neutron Bragg-edge transmission imaging of microstructures in bent steel plates," *Materials Science and Engineering: A*, vol. 675, pp. 19–31, oct 2016.
16. J. Huang, S. Vogel, W. Poole, M. Militzer, and P. Jacques, "The study of low-temperature austenite decomposition in a Fe–C–Mn–Si steel using the neutron Bragg edge transmission technique," *Acta Materialia*, vol. 55, pp. 2683–2693, may 2007.
17. M. A. Rodriguez, M. H. Van Benthem, D. Ingersoll, S. C. Vogel, and H. M. Reiche, "In situ analysis of LiFePO₄ batteries: Signal extraction by multivariate analysis," *Powder Diffraction*, vol. 25, pp. 143–148, jun 2010.
18. M. A. Rodriguez, D. Ingersoll, S. C. Vogel, and D. J. Williams, "Simultaneous In Situ Neutron Diffraction Studies of the Anode and Cathode in a Lithium-Ion Cell," *Electrochemical and Solid-State Letters*, vol. 7, no. 1, p. A8, 2003.
19. R. S. Kumar, X. Ke, J. Zhang, Z. Lin, S. C. Vogel, M. Hartl, S. Sinozaki, L. Daemen, A. L. Cornelius, C. Chen, and Y. Zhao, "Pressure induced structural changes in the potential hydrogen storage compound ammonia borane: A combined X-ray, neutron and theoretical investigation," *Chemical Physics Letters*, vol. 495, pp. 203–207, aug 2010.

20. H. Xu, Y. Zhao, D. D. Hickmott, N. J. Lane, S. C. Vogel, J. Zhang, and L. L. Daemen, "High-temperature neutron diffraction study of deuterated brucite," *Physics and Chemistry of Minerals*, vol. 40, pp. 799–810, nov 2013.
21. J. Eckert, O. Gourdon, D. E. Jacob, C. Meral, P. J. Monteiro, S. C. Vogel, R. Wirth, and H.-R. Wenk, "Ordering of water in opals with different microstructures," *European Journal of Mineralogy*, vol. 27, no. 2, pp. 203–213, 2015.
22. E. Zepeda-Alarcon, H. Nakotte, A. F. Gualtieri, G. King, K. Page, S. C. Vogel, H.-W. Wang, and H.-R. Wenk, "Magnetic and nuclear structure of goethite (α -FeOOH): a neutron diffraction study," *Journal of Applied Crystallography*, vol. 47, pp. 1983–1991, Dec 2014.
23. H. Xu, Y. Zhao, S. Vogel, L. Daemen, and D. Hickmott, "Anisotropic thermal expansion and hydrogen bonding behavior of portlandite: A high-temperature neutron diffraction study," *Journal of Solid State Chemistry*, vol. 180, pp. 1519–1525, apr 2007.
24. D. Luscher, J. Yeager, B. Clausen, S. Vogel, A. Higginbotham Duque, D. Brown, D. J. Luscher, J. D. Yeager, B. Clausen, S. C. Vogel, A. L. Higginbotham Duque, and D. W. Brown, "Using Neutron Diffraction to Investigate Texture Evolution During Consolidation of Deuterated Triaminotrinitrobenzene (d-TATB) Explosive Powder," *Crystals*, vol. 7, p. 138, may 2017.
25. H. E. Flotow, D. W. Osborne, and K. Otto, *The Journal of Chemical Physics*, **36**, (1962) 866.
26. J. W. Yang, T Gao, and L. Y. Guo, *Physica B* **429** (2013) 119-126.
27. P. A. Schultz, and C. S. Snow, *Modeling and Simulation in Materials Science and Engineering* **24** (2016) 035005.
28. M Zerkle, and J Holmes, *EPJ Web of Conference* **146** (2017) 13005.
29. C. J. Werner, J. Armstrong, F. B. Brown, J. S. Bull, L. Casswell, L. J. Cox, D. Dixon, R. A. Forster, J. T. Goorley, H. G. Hughes, J. Favorite, R. Martz, S. G. Mashnik, M. E. Rising, C. J. Solomon, A. Sood, J. E. Sweezy, A. Zukaitis, C. Anderson, J. S. Elson, J. W. Durkee, R. C. Johns, G. W. McKinney, G. E. McMath, J. S. Hendricks, D. B. Pelowitz, R. E. Prael, T. E. Booth, M. R. James, M. L. Fensin, T. A. Wilcox, and B. C. Kiedrowski, "MCNP User's Manual, Code Version 6.2," Tech. Rep. LA-UR-17-29981, Los Alamos National Laboratory (October 2017).
30. D. I. Poston, and H. R. Trellue, "User's Manual, Version 1.00, for MonteBurns, Version 3.01," Los Alamos National Laboratory document LA-UR-98-2718 (June 1998).
31. W.B. Wilson et al., "Recent Development of the CINDER90 Transmutation Code and Data Library for Actinide Transmutation Studies," *Proceedings of the International Conference*

on Future Nuclear Systems, GLOBAL '95, Versailles, France, American Nuclear Society, LaGrange Park, Illinois (1995).

32. H. R. Trellue, Alex Long, Erik Luther, Travis Carver, Vedant Mehta, "Effects of Hydrogen Redistribution at High Temperatures in Yttrium Hydride Moderator Material," submitted to *Journals of Materials* (2021) and Los Alamos National Laboratory report LA-UR-21-24178.
33. Shivprasad, A.P., Vogel, S.C., Mehta, V.K., Cooper, M.W.D., Saleh, T.A., White, J.T., Wermer, J.R., Luther, E.P. and Trellue, H.R., 2020. Thermophysical properties of high-density, sintered monoliths of yttrium dihydride in the range 373–773 K. *Journal of Alloys and Compounds*, p.156303.
34. M. Grosse, M. Van den Berg, C. Goulet, E. Lehmann, and B. Schillinger, *NIMA*, 651, 253 (2011).
35. M. Grosse, M. Van Den Berg, C. Goulet, and A. Kaestner, *J. Phys.: Conf. Ser.*, 340, 012106 (2012).
36. V. K. Mehta, et al., "A Density Functional Theory and Neutron Diffraction Study of the Ambient Condition Properties of Sub-Stoichiometric Yttrium Hydride," *Journal of Nuclear Materials* ; Vol.547, p.152837, 15 April 2021.
37. Vedant K. Mehta, Michael W.D. Cooper, Robert B. Wilkerson, Dan Kotlyar, Dasari V. Rao, Sven C. Vogel, "Evaluation of Yttrium Hydride (δ -YH_{2-x}) Thermal Neutron Scattering Laws and Thermophysical Properties," *Nuclear Engineering and Design*, submitted for publication, LA-UR-20-26691.
38. Vedant K. Mehta, Sven C. Vogel, Dan Kotlyar, Michael W.D. Cooper, "Direct Observatin of Bredig Transition in Yttrium Hydride (YH_{2-x})," pre-publication, LA-UR-20-26447.
39. Vedant Mehta, Michael W.D. Cooper, Dan Kotlyar, "Hydrogen Vacancy Effect on Yttrium Hydride (YH_{1.97}) Thermal Neutron Scattering Law," *Transactions of the American Nuclear Society*, Washington, D.C., Nov 17-21, Vol. 121.1, pp. 1358-1361, 2019.
40. Vedant Mehta, Patrick McClure, Dan Kotlyar, "Hydrogen Loss Effects on Microreactors for Space and Planetary Nuclear Power Production," *AIAA Propulsion and Energy Forum*, Indianapolis, IN, USA, AIAA-2019-4452, Aug 19-22, 2019.
41. Vedant Mehta, Patrick McClure, Dan Kotlyar, "Selection of a Space Reactor Moderator using Lessons Learned from SNAP and ANP Programs," *AIAA Propulsion and Energy Forum*, Indianapolis, IN, USA, AIAA-2019-4451, Aug 19-22, 2019.

42. J. Holmes, M. Zerkle, and D. Heinrichs, "Benchmarking a first-principles thermal neutron scattering law for water ice with a diffusion experiment," *EPJ Web of Conferences* **146**, 13004 (2017).
43. J.C. Armstrong, M.E. Rising, "MCNP Code Modernization & Code Improvement for Microreactor Multiphysics Calculations.", Tech. Rep. LA-UR-20-23568, Los Alamos National Laboratory, (May 2020).
44. J.C. Armstrong, K.C. Kelley, "Generating MCNP Input Files for Unstructured Mesh Geometries", Tech. Rep. LA-UR-20-27139, Los Alamos National Laboratory (September 2020).
45. V.K. Mehta, J.C. Armstrong, "Processing MCNP Elemental Edit Outputs", LA-UR-20-24025.
46. R. B. Wilkerson, et al., "MCNP Reactor Multigroup Tally Options Verification," Los Alamos National Laboratory report LA-UR-20-27819 (2020).
47. R. B. Wilkerson, "Advances in MCNP for Reactor Applications," Proceedings of American Nuclear Society Annual 2020 Meeting, Phoenix, Arizona, LA-UR-20-24067 (June 3-6, 2020).
48. H. R. Trellue, et al., "Demonstration of Advanced Experimental and Theoretical Characterization of Hydrogen Dynamics and Associated Behavior in Advanced Reactors," Los Alamos National Laboratory report LA-UR-20-22974 (April 2020).
49. H. R. Trellue, et al., "Simulation of Microreactor Design With Graphite Core Block, TRISO fuel, Heat Pipes, and Yttrium Hydride Moderator," Los Alamos National Laboratory report LA-CP-20-20306 (2020).

Appendix A. Changes Implemented to the MCNP Code and Associated Processing Steps

The new matprop elset name is introduced in an Abaqus input file. It is required that (i) each part with matprop element sets must have only one material element set, (ii) statistics and tally element sets are not allowed in the part that has matprop element sets, and (iii) a matprop element set cannot be combined with a material element set. The material elset names are used to map the material numbers in the part to the material numbers in the MCNP input file. The matprop element sets are used to group elements in the part based on densities and temperatures.

The routines in the `regl_abaqus_process.F90` and `regl_abaqus_utility.F90` files in the MCNP source code directory are used to process an Abaqus input file. An Abaqus input file is an ASCII file that contains a series of lines. Each line in the file cannot exceed 256 characters. If required data cannot be fit on a single 256-character line, then a comma (,) is placed at the end of the line to indicate that the next line is a continuation line. Three types of input lines are used in an Abaqus input file: comment lines, keyword lines, and data lines.

- Comments begin with double stars in column 1 and 2 (**). The comment lines are not used by the MCNP code.
- Keywords must begin with a star (*). The keyword lines may have parameters which appear as words or phrases separated by commas. The keyword must be followed by a comma if it has parameters. The parameters in a keyword line can stand alone or have values. If a parameter has a value, the equal sign (=) and double quotation mark (" ") are used to assign the value and to group the phrase value, respectively. Most keyword lines require one or more data lines.
- Data lines are generally used to provide data entries for the associated keyword options. If the data lines are required, they must immediately follow the keyword line. Data items are separated by commas. If there is only one item on a data line, it must be followed by a comma.

An Abaqus input file often begins with the heading keyword which is used to define a title for the analysis. The heading keyword and title lines are not required by the MCNP code. After the heading the input file contains the part definition blocks, assembly definition block, and material definition blocks. The following Abaqus keywords and associated data lines are used by the MCNP code: ***Heading**, ***Part/*End Part**, ***Assembly/*End Assembly**, ***Instance/*End Instance**, ***Node**, ***Element**, ***Elset**, ***Material**, and ***Density**. All part definition blocks must be defined before the assembly definition block and material definition blocks. The assembly block and material blocks may appear in any order after the part blocks.

The `readAbaqusFile` routine is to read an Abaqus input file, and then extract the mesh metadata related to geometries and materials. First, the number of parts, instances, and materials are extracted from the corresponding keyword lines. Second, the number of nodes, elements, and elset in each part are computed from the associated data lines. Third, the part and instance data are used to compute the number of pseudo-cells. The metadata are needed to allocate arrays in

which mesh and material data will be stored. The processAbaqusData routine is to (i) process node, element, elset data and store into the arrays, and (ii) to construct the pseudo-cells based on the part and instance data. The MCNP code uses the mesh and material data to construct the global geometry model where particles are tracked.

Process followed by MARM:

- I. Model and mesh a solid geometry to get an ABAQUS input file
- II. Run ABAQUS with guess heat flux
- III. Read ODB to construct ABAQUS and MCNP input files to run MCNP at time step t_0 [write_mcabq_inputs.py]
 1. Run MCNP
 2. Read MCNP output and EEOU files to construct an ABAQUS input file [mcnp_to_abaqus.py]
 3. Run ABAQUS
 4. Extract temperatures at elements from an ABAQUS run and density at elements from a MCNP run [extract_matprop.py]
 5. Use material properties (temperatures and density) at elements and mesh geometry from an ODB file to write new ABAQUS and MCNP input files [write_mcabq_inputs.py]
 6. Repeat Step 1-5 until a terminating condition is met.
 - go to Step 1 using the new Abaqus and MCNP input files (from Step 5)

Selective element set generation can occur using MARM is shown below in Figures 18 and 19 through the following tasks: 1) need to generate element sets based on temperature / density / stoichiometry, etc., 2) element sets correspond to mat-prop pseudo cells in MCNP, 3) set generation must be on a per-instance basis, and 4) additional physics needed for set generation, i.e., Stoichiometry changes due to temperature.

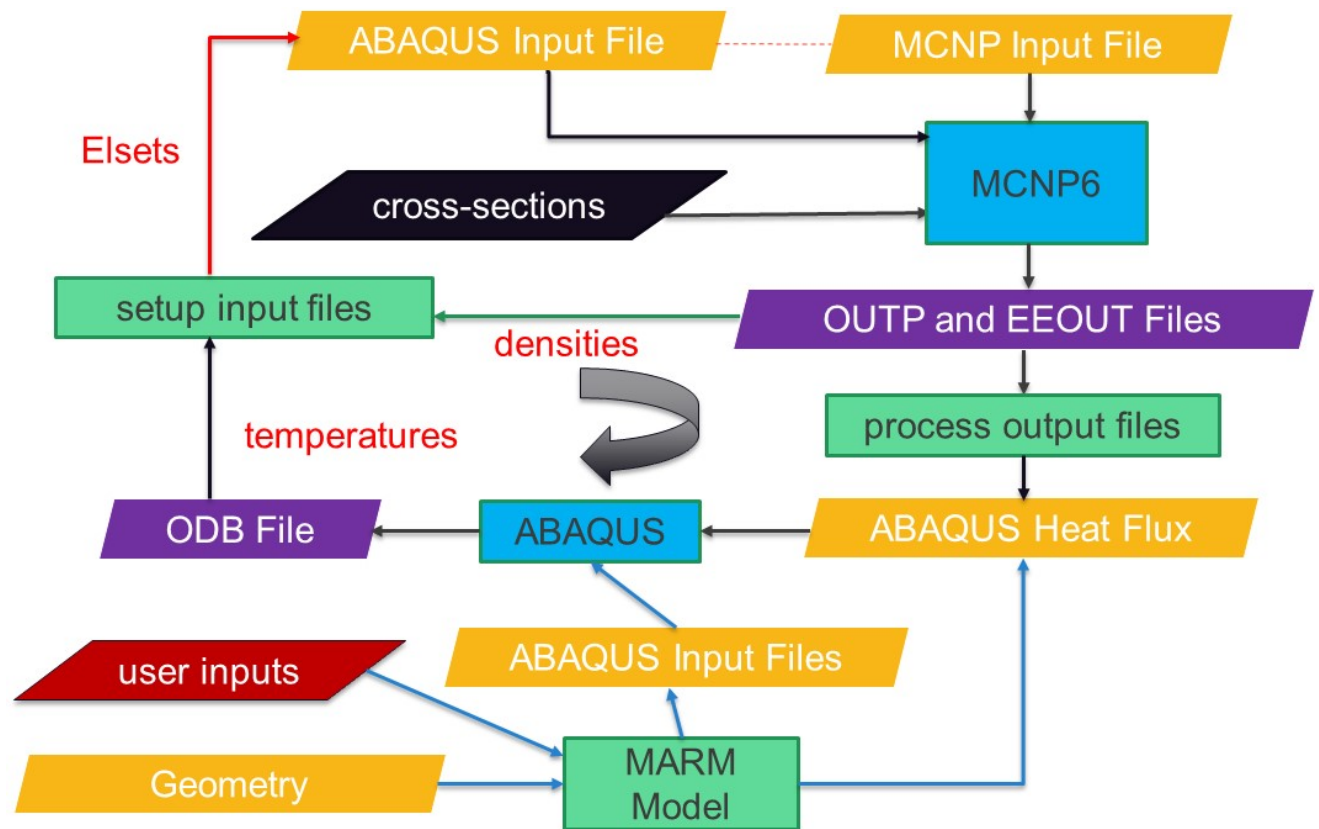


Figure 18. Python Implementation for MARM

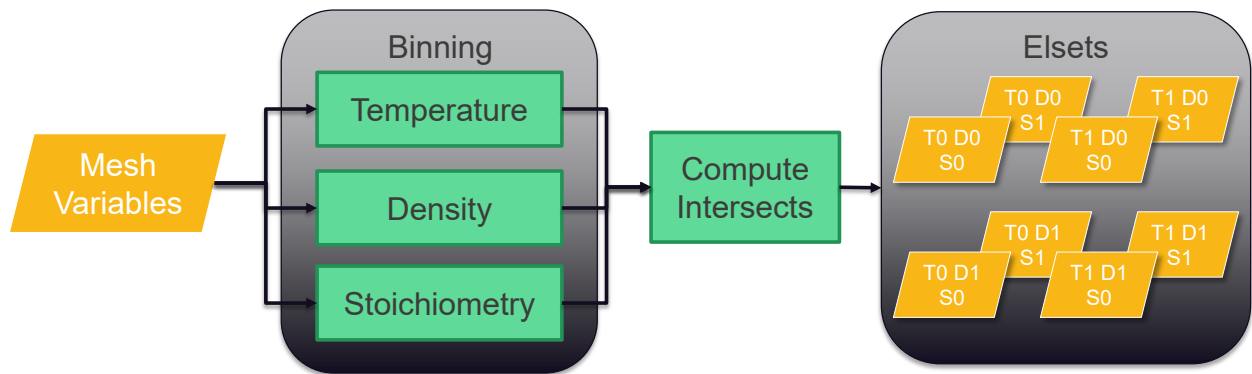


Figure 19. Selective Element Set Generation